

A VLT/NACO Study of Star Formation in the Massive Embedded Cluster RCW 38¹

K.L. DeRose, T.L. Bourke, R.A. Gutermuth and S.J. Wolk

Harvard-Smithsonian Center for Astrophysics, 60 Garden Street, Cambridge, MA 02138

S.T. Megeath

*Department of Physics and Astronomy, The University of Toledo, 2801 West Bancroft
Street, Toledo, Ohio 43606*

J. Alves

*Centro Astronómico Hispano Alemán, C/Jesús Durbán Remón 2-2, E-04004 Almería,
Spain*

and

D. Nürnbergger

European Southern Observatory, Casilla 19001, Santiago, Chile

ABSTRACT

We present the results of high angular resolution adaptive optics (AO) near-infrared (JHK_s) observations of the deeply embedded massive cluster RCW 38 using NACO on the VLT. Narrowband AO observations centered at wavelengths of $1.28\ \mu\text{m}$, $2.12\ \mu\text{m}$, and $2.17\ \mu\text{m}$ were also obtained. The area covered by these observations is about $0.5\ \text{pc}^2$, centered on the O star RCW 38 IRS2. We use the JHK_s colors to identify young stars with infrared excess in this region. Through a detailed comparison to a nearby control field, we find that most of the 337 stars detected in all three infrared bands are cluster members (~ 317), with essentially no contamination due to background (likely due to the high cluster extinction of $A_V \sim 15$) or foreground sources. Five sources with 3 band detections have colors suggestive of deeply embedded protostars, while 53 sources are detected at K_s only; their spatial distribution with respect to the extinction suggests they are highly reddened cluster members but their evolutionary status is unclear. Detectable K_s -band excess is found toward $29 \pm 3\%$

of the stars. For comparison to a similar area of Orion Nebula Cluster observed in the near-infrared, mass and extinction cuts are applied, and the excess fractions redetermined. The resulting excesses are then $25 \pm 5\%$ for RCW 38, and $42 \pm 8\%$ for Orion. RCW 38 IRS2 is shown to be a massive star binary with a projected separation of ~ 500 AU. Two regions of molecular hydrogen emission are revealed through the $2.12 \mu\text{m}$ imaging. One of these shows a morphology suggestive of a protostellar jet, and is clearly associated with a star only detected at H and K_s , and previously identified as a highly obscured X-ray source. Three spatially extended cometary-like objects, suggestive of photoevaporating disks, are identified, but only one is clearly directly influenced by RCW 38 IRS2. The structure of the inner core of RCW 38 is also characterized and compared to Orion and other clusters. A King profile provides a reasonable fit to the cluster radial density profile and a nearest neighbor distance analysis shows essentially no sub-clustering.

Subject headings: stars: formation – infrared: stars – ISM: individual (RCW 38)

1. Introduction

The study of embedded clusters is vital to our understanding of star formation because most stars have been shown to form in large clusters with hundreds of stars (Lada & Lada 2003, Porras et al. 2003, Carpenter 2000 and Allen et al. 2007). Of particular interest are the largest clusters with thousands of stars because it is in these clusters where large numbers of low mass stars live in close proximity to luminous O-stars. In the Lada & Lada 2003 tabulation of clusters within 2 kpc, there are two such larger embedded clusters with over 1000 stars: the Orion Nebula Cluster (ONC) and RCW 38 (Wolk et al 2006). The other clusters within 1 kpc typically contain only a few hundred stars, making direct comparisons with the ONC not possible. It is even likely that our Sun was formed in such a cluster. A possible explanation for the abundances of many radioactive isotopes in our Solar System is the presence of a nearby supernova during its formation which would have been a more probable occurrence in a rich cluster like the ONC or RCW 38 (Meyer & Clayton 2000).

Studying embedded star clusters not only yields important information regarding the formation and evolution of stars, it also yields important information regarding the formation

¹Based on observations performed at the European Southern Observatory Very Large Telescope on Cerro Paranal, Chile, under program ID 70.C-0400(A).

and evolution of planetary systems around these stars. As first studied in the Orion Nebula Cluster (ONC), protoplanetary disks (PROtoplanetary DiskS) exist as large disks of dust and gas that provide material for future planet formation. However, when exposed to unattenuated ultraviolet (UV) radiation the molecular hydrogen dissociates causing the outer portions of the disk to photoevaporate (Hollenbach et al. 1994). Since many young low-mass stars in other regions exist in close proximity to massive OB stars that output a significant amount of UV radiation, it is important to determine whether this process seriously inhibits planet formation around them. Low-mass stars are important because they represent the majority of young cluster members, which means the vast majority of planets may be formed around them. Thus, low-mass stars clustered around OB sources are at the same time the most likely to form planets and the most likely to experience photoevaporation effects. Knowledge of the disk frequency in a cluster as a function of the distance from the massive OB stars can constrain the affect of photoevaporation on disk evolution (Balog et al. 2007). Such knowledge will help to constrain the conditions that are necessary for those disks to evolve into planets.

The HII region RCW 38, at a distance of 1.7 kpc (Beck, Fischer & Smith 1991), contains an embedded cluster centered around a O5 star IRS2. RCW 38 is more embedded than the ONC and due to the OB stars in the center it provides a similar environment for the study of disk photoevaporation and evolution. Smith et al. (1999) showed that the winds from IRS2 have created a 0.1 pc bubble that is relatively free of dust, leaving stars within the bubble directly exposed to UV radiation. This bubble is filled with diffuse thermal and synchrotron X-ray emission (Wolk et al. 2002) and the intersection of the central gas bubble with the surrounding dust cloud appears to be a site of active star formation (Smith et al. 1999).

Wolk et al. (2006) observed the central region of RCW 38 at X-ray and near-infrared wavelengths, identifying a large cluster population of 360 X-ray sources that are likely cluster members over the total field down to $\text{Log}[L_x] \sim 30$. Comparing this to the COUP (Chandra Orion Ultradeep Project) measurements of the ONC discussed in Feigelson et al. (2007), roughly 200 sources of their sample are more luminous than $\text{Log}[L_x] \sim 30$. The number of sources in the COUP measurement is on the same order as Wolk et al. (2006). The somewhat larger numbers in the latter study may be explained by the larger physical area surveyed relative to the former. Since the ONC and RCW 38 have similar populations of young stars, this shows that both the ONC and RCW 38 are unique large clusters within 2 kpc. For the central region of RCW 38, Wolk et al. (2006) determined that 97% of the ~ 200 X-ray sources within $200''$ of IRS2 are likely cluster members. In this region they determine that the disk fraction is 49% from near-infrared (JHK_s) excess measurements. The infrared observations of Wolk et al. (2006) of the central $2'.5$ of the RCW 38 cluster were performed with ISAAC at the Very Large Telescope (VLT), with resolution insufficient to resolve close sources in

the most crowded region around the O5 star. We present here the results of our observations of the central $\sim 1'$ of RCW 38 with adaptive optics near-infrared imaging with the NACO system on the VLT, which allow us to better separate close sources and to separate the source emission from the nebular background emission, providing a sample that is more easily compared to the nearer ONC. In §2 we describe the observations, in §3 we discuss the photometry and completeness limits, and in §4 we present the results on infrared excess sources, cluster membership, the central O star, protostellar candidates, molecular hydrogen emission, proplyd candidates, and the disk fraction. In §5 we analyse these results, discussing cluster structure and the effect of the O stars on disks around low mass stars. Our summary is presented in §6.

2. Observation and Data Reduction

2.1. NAOS-CONICA

High angular resolution near infrared imaging of RCW 38 was performed on February 20, 2003 and February 23, 2003 using NAOS-CONICA (NACO) at Yepun, one of the 8.2 m unit telescopes of the Very Large Telescope (VLT) installed at the European Southern Observatory’s (ESO) site on Cerro Paranal, Chile. NAOS (Nasmyth Adaptive Optics System) is an adaptive optics (AO) system that assists imaging at wavelengths in the range 0.8–5.5 μm by directing light from the telescope partially into a (either optical or infrared) wavefront sensor. The remaining light is directed into the CONICA infrared camera that is equipped with a 1024×1024 pixel Aladdin InSb array detector (Lenzen et al. 2003; Rousset et al. 2003).

The CONICA S54 setup (pixel scale $\sim 0''.054$; instantaneous field-of-view $\sim 56'' \times 56''$) was used to take 3 sets of 14 frames each in the broad-band J , H and K_s filters, centered at a wavelength of 1.27 μm , 1.66 μm and 2.18 μm , respectively. In addition, 3 sets of 12 frames each were taken in narrow-band filters centered at the following wavelengths: 1.28 μm (bandwidth = 0.014 μm), 2.12 μm (bandwidth = 0.022 μm) and 2.17 μm (bandwidth = 0.023 μm), covering the $Pa\beta$, H_2 (1–0) S(1), and $Br\gamma$ lines, respectively. Detector integration times (DITs) and NDITs are given in Table 1. The integration time per frame is $\text{DIT} \times \text{NDIT}$.

Wavefront sensing was performed with the IR sensor to close the AO loop on the bright infrared source RCW 38 IRS 2 (self-referencing) at $\text{RA} = 08^{\text{h}}59^{\text{m}}05''.5$, $\text{DEC} = -47^{\circ}30'39''.4$ (J2000), and $\text{SpT} = \text{O5V}$ (Frogel & Persson 1974; Smith et al. 1999). The airmass ranged from 1.15 to 1.30 during the observations. For both nights, observing conditions were exceptionally good and stable, with a clear sky and optical seeing mostly in the range $0''.4$ – $0''.6$. As

measured on the obtained data sets themselves, the image quality (i.e., the median FWHM PSF of randomly selected point sources) is found to be better than $0''.2$ for all six filter settings.

To allow corrections for cosmic rays and bad pixels, a jitter pattern (random offsets within a jitter box of width $2''$) was applied, resulting in a total field of view of $60''.8 \times 58''.3$. This corresponds to linear scales of $0.5 \text{ pc} \times 0.48 \text{ pc}$ at the distance of 1.7 kpc . Twilight flats, lamp flats and dark frames were taken through the usual NACO calibration plan. For each individual frame, all basic steps of data reduction (i.e., flat-fielding, sky subtraction and bad pixel correction) were performed using standard routines within the IRAF software package. For an exhaustive description of the processing of crowded field IR data we refer to Nürnbergger & Petr-Gotzens (2002). Figure 1 shows the final data set as a combined 3-color image.

2.2. SOFI Control Field

In order to estimate the degree of background contamination, a control field (J. Ascenso, private communication) was imaged on June 17, 2005 in the J , H , and K_s passbands using the SOFI (Son of ISAAC) on the NTT (New Technology Telescope) at La Silla, Chile. The resolution of the image is approximately 0.29 arcsec/ pixel and centered at $10^{\text{h}}18^{\text{m}}01^{\text{s}}.2$ and $-57^{\circ}15'31''.1$. A total of 6 frames per passband were combined together, resulting in an integration time of 36 s per band. The total FOV is approximately $4' \times 4'$.

3. Source Identification and Photometry

3.1. PhotVis Identification

Point source detection and photometry was accomplished using Gutermuth’s IDL photometry and visualization tool, PhotVis version 1.10 (Gutermuth et al. 2008). PhotVis selects point sources from embedded regions containing significant amounts of nebulosity with a modification to the standard DAOPhot algorithm. PhotVis is heavily dependent on the FITS procedures and DAOPhot version 1 port supplied by the IDL Astronomy Users Library (Landsman 1993).

Gaussian distributions were assumed for all sources and sources with a full-width at half-maximum (FWHM) greater than 2.5 pixels ($0''.135$) were discarded. The images were also visually inspected to remove false positives due to image artifacts. Flux measurements

were taken using a 3 pixel ($0.162''$) radius and background measurements were determined using inner and outer sky annuli of 5 pixels ($0''.27$) and 8 pixels ($0''.432$) respectively. This procedure was used to perform relative photometry on both NAOS-CONICA data and the SOFI control field. Absolute photometry was not performed on the NACO narrow band images.

3.2. Completeness and Detection Limits

Differential completeness limits of 90% were calculated in all images by inserting successively fainter fake stars with gaussian profiles and FWHM equivalent to those in the image and taking 90% of the false sources recovered. For this test, sources with magnitude errors greater than 0.2 were discarded as well as sources that deviated in brightness by 3σ more than the original (due it being overlayed over a brighter source). Final values for the completeness limits of the NACO data are $J=19.01$ mag, $H=18.13$ mag, and $K_s=16.97$ mag. Detection limits (5σ) in these bands are $J=20.3$ mag, $H=19.0$ mag, and $K_s=18.0$ mag. The 90% completeness limit for the SOFI control field calculated in the same manner is $K_s=15.67$ mag. J and H completeness limits were not calculated because only the K_s -band control field was necessary for background contamination estimates. The saturation limits for both fields was approximately 11th magnitude in all 3 passbands.

Utilizing the J and H completeness limits yields a mass detection limit of $0.12 M_\odot$ at 1 Myr for an average extinction of $A_V = 10$ ($A_K = 1.1$; Rieke and Lebofsky 1985). The mass detection limit was approximated using the Baraffe 1 Myr isochrone (Baraffe et al. 2002) and the distance modulus of 11.15 calculated with the assumed distance of 1.7 kpc. This detection limit is right above the hydrogen burning limit of $0.08 M_\odot$, so there are no brown dwarf candidates in the NACO sample.

3.3. NAOS-CONICA Calibration

The NACO WCS and zero-point flux calibrations were performed using larger FOV images of RCW 38 obtained with ISAAC (Infrared Spectrometer And Array Camera) on the VLT. We used the photometry extracted from the ISAAC data by Ascenso (2008). Due to the use of PSF fitting and to a better estimate of the sky contribution on the nebulous background, the Ascenso (2008) photometry is believed to be more reliable than the aperture photometry of Wolk et al. (2006). The ISAAC data was registered and calibrated using sources from the 2MASS Point Source Catalog in the larger ISAAC field. The SOFI control

field was flux and position calibrated using 2MASS sources at measurements up to magnitude 14 in JHK_s , due to the fact that the SOFI field is much deeper. All sources in all images with a measured uncertainty greater than 0.2 magnitudes (outside of 1σ) have been discarded.

In addition, because the AO feedback loop was closed using a central source for the NACO data, there is a significant amount of off-axis elongation in many sources in the images. This caused a linear trend in magnitude difference between the ISAAC and NACO photometric measurements as a function of radial distance from IRS2. We therefore used position dependent zero points given by the equations:

$$\begin{aligned}
 J &: 24.426 - 0.0176 \times r_{\text{off}} \\
 H &: 22.828 - 0.0247 \times r_{\text{off}} \\
 K_s &: 21.648 - 0.0274 \times r_{\text{off}}
 \end{aligned}
 \tag{1}$$

where r_{off} is the radial offset from IRS2 in arcseconds.

4. Results

4.1. Color-color and Color-magnitude Diagrams

The infrared photometry for the 483 sources detected in at least one band with a magnitude uncertainty of < 0.2 is listed in Table 3. The number of sources detected in each of the three broad-bands are shown in Table 2. We detected 409 sources in H and K_s and 344 sources in all bands with uncertainties < 0.2 magnitudes. This uncertainty cutoff results in average photometric errors of 0.07 mag for J and 0.06 mag for H and K_s . Inspection of the 344 sources detected in JHK_s shows that seven sources have $(J - H)$ values less than 1 magnitude and deviated significantly from the bulk of the sample. Of these seven, four have a K_s -band excess. Upon visual inspection, it was evident that two of these sources had an excess of flux detected in J due to artifact contamination in that image (where residual images of the central source IRS2 can be seen in multiple places in the central portion of the image). Along the same lines, four of the other sources were very near IRS2 or partially obscured by a much larger, brighter star, which explains the excess flux detected in J . The final source, that remains unexplained by the previous explanations, is likely a foreground source (especially due to the fact that it does not show K_s -band excess) and thus, is not a cluster member. Of the seven sources, six have incorrect photometry, and are tagged in Table 3 with an ‘x’. These sources have been omitted from the final data set, leaving the

total number of JHK_s sources at 337. It is this data set of 337 sources that is used for the rest of the analysis in this paper. The color-color diagram for these sources is shown in Figure 2 and the color-magnitude diagram in Figure 3.

4.2. The IRS2 O Star Binary

IRS2, the central source of RCW 38, has been previously thought to be a single source, but with the increase in resolution enabled by the AO system, it is possible to show that it is in fact a binary system. The separation of the two sources can be confirmed in all three broad-bands through visual inspection, but due to the brightness of the two sources, the detector is saturated in this region for the broadband JHK_s filters. Therefore, the narrowband images ($2.17\mu\text{m}$ and $2.12\mu\text{m}$) have been used for a relative photometric analysis of IRS2. The ratio of the detected flux from the brightest pixel in each source shows the dimmer source to have $\sim 94\%$ of the flux of the brighter source (89% in the case of the $1.28\mu\text{m}$ image). Comparing this ratio to the ratio of Lyman continuum photons given for various ZAMS spectral types in Panagia (1973; Martins et al. 2005), shows that both stars in the binary should have the same spectral type. Figure 4 shows magnified images of IRS2 with contours in these two bands. From the narrowband images, the projected separation between the two sources is $0''.27$ which is 459 AU at 1.7 kpc.

Smith et al. (1999) address the question of the effective temperature and hence spectral type of IRS2 by treating it as a single source and fitting nebular spectroscopic lines to models of HII regions using stars with Kurucz stellar atmosphere models, from which they determine an effective temperature in the range of 43000K to 48000K. Smith et al. favored the lower range for IRS2, 43000 – 44000 K, corresponding to a spectral type of O5 – O5.5 (Panagia 1973), but not ruling out a temperature of 48000 K, corresponding to an O4.5 spectral type. More recent modelling suggests the lines used by Smith are very sensitive to model parameters, and after an effective temperature of 40000K, the lines are rather insensitive (Mokiem et al. 2004). Therefore, a new look at Smith et al. suggests only that the effective temperature is greater than 40000K.

The ionizing flux can be measured independently at radio wavelengths. At 5 GHz, Wilson et al. (1970) measured a flux of 172 Jy (over a large area with a $4'$ beam), while Vigil (2004) measured 99 Jy (with a $10''$ beam interferometrically) at the same frequency. The Vigil (2004) observations focused on the immediate region around IRS2, and is likely to be more representative of the flux solely due to IRS2.

Taking the electron temperature to be 7500 K (Caswell & Haynes 1987), and assuming

the Wilson et al. and Vigil results represent the upper and lower limits respectively, we find that the number of Lyman continuum photons, N_L , is in the range $2.7 - 4.7 \times 10^{49} \text{ s}^{-1}$ (Armand et al. 1996), or $\log(N_L) \sim 49.1 - 49.4$. Following Martins et al. (2005) this range of $\log(N_L)$ values implies a spectral type of O4 to \sim O5.5 for luminosity class (LC) V stars, and O5.5 to O7 for LC III stars. For an effective temperature $\geq 40000 \text{ K}$, the calibration of Martins et al. (2005) suggests a spectral type of O5.5 or earlier for LC V and O5 or earlier for LC III. Therefore, the radio flux and effective temperature measurements give inconsistent results for LC III, while for LC V they are consistent. Further, as these are young stars, LC V is more likely, and thus we conclude that the spectral types of the IRS2 binary, which we assume to be of equal mass, are likely to be \sim O5 V, with a range of O4-O5.5 consistent with the available data. Note that the other OB star candidates in the immediate vicinity of IRS 2 have $\log(L_{bol}) \leq 3.4$ (Wolk et al. 2006), and thus are not likely to contribute significantly to the continuum radiation.

4.3. Cluster Membership

Completeness histograms of H and K_s magnitudes do not show the characteristic steep rise towards the fainter magnitudes that is often present due to background sources if the cloud is being penetrated. This implies that the region is relatively free from extensive background contamination to the depth of our survey (Carpenter et al. 1997), but the likelihood of a small fraction of the detections being from background sources is estimated from the SOFI control field.

An extinction map for the NACO field was calculated following the method of Guter-muth et al. (2005) and is shown in Figure 5. We used $H - K_s$ colors for groups of the 20 closest sources detected in all bands, sampled at each point in a uniform grid with a spacing of $3''.7$, in order to analyze the extinction surface density. The reddening law of Rieke and Lebofsky (1985) was used. Sources used are all sources detected in H & K_s with $\sigma < 0.2$. It is important to note that the measurements used to make this extinction map are dominated by cluster members, and so it is mostly a map of the extinction in front of and intrinsic to the cluster.

The NACO extinction map yields a mean extinction of $A_V = 14.8$, which is a much higher extinction than the SOFI field due to the molecular cloud. The average extinction in the SOFI K_s -band control field is $A_V = 1.83$, which was calculated as described above for the NACO field. Therefore, for comparison, the control field K_s -band magnitudes were artificially extinguished by $A_K = 1.45$ magnitudes. This is an underestimate of the reddening, thus the amount of contamination should be considered an upper limit. The extinguished

sample yields a 90% completeness limit of 17.12 magnitudes for the control field compared to 16.97 for the RCW 38 field.

Figure 6 shows K_s magnitude histograms (regardless of a detection or lack of at J and/or H) for the NACO RCW 38 data, the artificially extinguished control field data scaled by area, and the “corrected” histogram given by their subtraction. The total FOV of the control field is $4'2 \times 4'2$ and the area covered in the NACO observations is only 5.8% of this, which gives the area scaling factor. Integrating over the bins brighter than the NACO 90% completeness limit cutoff and using \sqrt{n} counting statistics to calculate error, the histogram shows 424 total NACO K_s -band sources and $N_{bkgd} = 20 \pm 2$ control field sources (scaled by the area ratio) so that 4.7% of the NACO sources are potential background contaminants. Therefore, of the 337 JHK_s sources (including protostellar candidates), 317 ± 5 sources can be considered cluster members. This estimate of background contamination should represent an overestimate because the number of reddened background stars is reduced by requiring J and H detections as well. Because the contamination from background sources is small, all 337 sources are included in the analysis and diagrams of this paper, except for the disk fraction analysis where the corrected total of 317 ± 5 sources is used.

The small amount of contamination is due to two reasons. One is simply the small field-of-view of our observations, combined with the extinction in front of and intrinsic to the cluster, of $A_V \sim 15$. The other is the large background column density, as derived from observations of the thermal dust continuum near 1-mm wavelength (Cheung et al. 1980). The peak column density is measured to be $8 \times 10^{23} \text{ cm}^{-2}$, corresponding to an extinction of $A_V = 400$ (Wolk et al. 2006). Thus it appears that the embedded cluster lies in front of a dense molecular cloud whose high extinction screens out background sources.

4.4. Candidate Protostars and K_s -band only Sources

There are five JHK_s sources whose 1σ error bars in both coordinates of color-color space fall completely outside the reddening vector extending from the T-Tauri locus in Figure 2. These are protostellar candidates identified in a similar way as Lada & Adams (1992), and they represent approximately 2% of the population. They are tagged in Table 3 with a ‘p’. These candidates were visually inspected and appear to be true detections. Lada et al. (2000) find that protostellar candidates compose 13% of sources detected in $JHKL$ in the Trapezium Cluster, with the difference likely due to the additional L -band sensitivity represented in the Lada et al. data set.

There are also 53 sources with magnitude error less than 0.2 that were detected in K_s -

band only. These sources are mostly cluster members due to the small amount of background contamination as shown in Figure 6. These sources could either be highly extinguished T-Tauri stars or protostellar candidates. We have compared their distribution to the extinction map shown in Fig 5, and we find that most of the sources are located in regions of high extinction. In Figure 1 these sources are clearly seen in the east and south-east as red sources. There are also 65 sources with magnitude error less than 0.2 that were detected in H and K_s -band only. These sources are distributed in a similar way to the sources only detected in the K_s -band, suggesting they are likely extinguished T-Tauri stars or embedded sources.

4.5. Molecular Hydrogen Emission

Narrowband imaging of the H_2 1-0 S(1) line at $2.122 \mu\text{m}$ is often used to identify shocked molecular emission due to outflows. In a nebulous region such as RCW 38, pure H_2 line emission must be distinguished from the extensive and bright continuum emission using multi-band data. By comparing the $2.122 \mu\text{m}$ narrow-band image with the broad-band K_s image, two regions of H_2 emission have been identified (Fig. 7). Both lie along the IRS 1 ridge, which has previously been identified as a region of active star formation (Smith et al. 1999; Wolk et al. 2006). Region A in Fig. 7 shows H_2 emission extending to the SW from an infrared point source that is one of the redder sources in the region (No. 174 in Wolk et al. 2006). This infrared source is coincident with one of the brighter X-ray sources (over 500 counts) but is barely detected at J in the NACO data. It is likely to be an embedded protostar with an outflow.

In region B, H_2 emission extends to the SW from a kink in the IRS 1 ridge emission, suggestive of a relationship between the two features. No infrared point source can be directly associated with this emission however, and so its origin is unknown. A deeply embedded protostar may be waiting to be found in this region, perhaps through deep mid-infrared imaging and/or through interferometric imaging at millimeter wavelengths. Unlike the ONC (Kristensen et al. 2003; McCaughrean & Mac Low 1997; Allen & Burton 1993), or a large number of small scale outflows from the cluster members (Davis et al. 2008), there is no large scale H_2 emission in the RCW 38 region that could be suggestive of a recent explosive event, or a large number of small scale outflows from the cluster members.

4.6. Photoevaporating Disks

The narrowband imaging reveals three candidate photoevaporating disks – stars with cometary-like head-tail morphologies (Figs. 8, 9, 10, 11). While all have stellar-like point sources at their heads, only one of these is clearly directly affected by IRS 2, with its tail pointing directly away from the O-star and lying in close proximity (Fig. 9). These objects are well seen in the narrowband images at $2.12 \mu\text{m}$ (H_2) and $2.17 \mu\text{m}$ ($\text{Br}\gamma$), when compared to the broadband images at H and K_s that are dominated by continuum emission. The proplyds in Orion have typical sizes $0''.15$ to $1''$ (O’dell 1998), which translates to 62–413 AU assuming the distance to the ONC is 414 ± 7 pc (Menten et al. 2007). Our observations have a pixel scale of $0''.054$ (91 AU at a distance of 1.7 kpc), which should allow for the identification of any larger Orion-like proplyds in the region. We have detected at most three similar objects with tail sizes that are approximately 1275 AU (Fig. 10) and 2208 AU (Figs. 9, 11). It is interesting to note that two of these objects are located in the IRS 1 ridge. One of the goals of undertaking both narrowband and broadband imaging was to identify both resolved and unresolved proplyds. In the case the proplyds are unresolved, they would be identified as sources of line emission in the narrowband images after careful subtraction of the continuum (broadband) emission. However, the variable PSF, both in time and across the FOV, make such a comparison difficult if not impossible, and we have not attempted to do this. Stable PSFs like those provided by space-based platforms are needed to undertake a search for unresolved emission from evaporating disks.

4.7. Disk Fraction

Using the $(J - H)$ vs. $(H - K_s)$ color-color diagram (Figure 2), it is possible to isolate 87 sources (92 including protostellar candidates) with K_s -band emission greater than that expected for a stellar photosphere. These sources are tagged in Table 3 with an ‘e’ for excess sources, and a ‘p’ for protostellar candidate. Figure 5 shows a spatial distribution of these sources and Figure 12 shows a histogram of sources vs. radial distance from IRS2. Excess infrared emission is often indicative of the presence of inner disks. The disk fraction D is calculated as:

$$D = \frac{N_{excess}}{N_{tot} - N_{bgd}} \quad (2)$$

where N_{excess} is the number of sources with an infrared excess, N_{tot} is the total number of sources, and N_{bgd} is the number of background sources. The disk fraction as a function of

radial distance from IRS2 is plotted in Figure 13. In this manner we find a disk fraction of $29 \pm 3\%$. The disk fraction is quoted without mass and extinction limited sampling because it did not affect the final value. We perform mass and extinction limited sampling when comparing RCW 38 and the ONC. This is a lower fraction than found in similar studies (JHK) of similar clusters (Lada et al. 2000; Haisch et al. 2000; Hillenbrand 2005), given its degree of embeddedness ($A_V \sim 10$) and inferred young age (0.5 Myr; Wolk et al. 2006).

As mentioned previously, RCW 38 is an interesting region to study in that we are able to compare what we find to the best studied young cluster, the ONC, to see if the trends found there exist elsewhere. Lada et al. (2000) in their $JHKL$ survey of the ONC covering approximately the same linear scale as our RCW 38 study (a 0.4 pc square region) found a disk fraction of $50 \pm 7\%$ determined by K_s -band excess, while a disk fraction of $80 \pm 7\%$ was determined using L -band excess. Both K_s and L are sensitive to warm inner disk emission (≤ 1 AU) and require favorable angles of inclination, inner disk holes, and accretion rates for detection (Lada et al. 2000). However, the photospheric emission of a given star has a lower intensity in L rather than K_s , which means the K -band excess must compete with photospheric emission much more than L -band. Thus, longer wavelengths such as the L -band, that can more reliably detect disks, resulting in higher disk fractions than for studies relying on K_s -band excess only, are needed. It is highly likely that our survey of RCW 38 only detects a fraction of disks present. The only way to test this would be to image the region in L -band or longer wavelengths with sufficient sensitivity and resolution to resolve individual sources, which is a difficult task for a cluster at 4 times the distance of the ONC (1.7 kpc) with bright nebulosity.

The disk fraction of $50 \pm 7\%$ found for the ONC using K_s -band excess is difficult to directly compare to the present result due to differences in sensitivities and photometric techniques. In order to make a fairer comparison, the JHK_s data on the ONC from Muench et al. (2002) was obtained and a $0.3 M_\odot$ mass cut and a $(J - H) < 2$ extinction cut applied to both data sets, over the same linear region. This resulted in 218 sources in the ONC, including 71 excess sources, and 112 sources in RCW 38, with 28 excess sources. The overall disk fractions for the two data sets subjected to these cuts are $25 \pm 5\%$ for RCW 38 and $42 \pm 8\%$ for the ONC. These fractions are significantly different, for reasons unknown. As noted, however, determining the infrared excess fraction from JHK data only is likely to underestimate the true fraction (Lada et al. 2000).

5. Analysis

5.1. Photoevaporating Disks?

Sources with disks in RCW 38 seem to be evenly distributed throughout the region, with the majority of disks found between 0.07 and 0.17 parsecs from IRS2 (48%, compared with only 24% at smaller distances). Because of the UV radiation emanating from the massive O-star binary IRS2, it might be expected that the disks nearest to the central source would have been evaporated. Photoevaporating disks in the inner region of a cluster have been well documented in the Trapezium Cluster on account of the O star θ^1 C Ori through both radio observations (Churchwell et al. 1987; Felli et al. 1993) and both ground and space based optical imaging (Laques & Vidal 1979; O’dell, Wen, & Hu 1993). Instead of a deficit of disks near IRS2, we find a slight increase in disk fraction with decreasing projected distance from IRS2 (Fig 13). However, the physical separations are not known and the proximity of some of these stars to IRS2 could be a projection effect. In addition, since the cluster is quite young and thus dynamically active, stars moving at 1 km/s would move across the entire FOV in just 0.5 Myr, making it nearly impossible to tell which stars have spent prolonged amounts of time near IRS2. This could explain the apparent lack of resolved proplyd-like objects in the inner region near to IRS2.

It is also possible that the outer disks of many of these sources have been blown away, leaving the inner disks intact which is the portion most sensitive to K_s -band measurements. O5.5 stars such as IRS2 emit large quantities of Far-Ultraviolet (FUV) and Extreme-Ultraviolet (EUV). More FUV radiation is emitted than EUV radiation, which means that FUV radiation is the dominant cause of photoevaporation because it works to evaporate the outer portions of the disks at a faster rate. EUV radiation works to evaporate the disk at a slower rate, so when the outer portion of the disk has been photoevaporated from FUV radiation, it is the more energetic EUV radiation that slowly works to cook away the inner disk. Adams et al. (2006) modeled this photoevaporation effect for embedded clusters with varying memberships. They define a G_0 term given in units of the typical interstellar radiation field at FUV wavelengths (given as 1.6×10^{-3} ergs s^{-1} cm^{-2}). For an O star binary (assuming a temperature of 41000K and $R_\star = 15R_\odot$), sources at 0.01 pc would experience $G_0 = 43000$ which decreases as $1/(\text{distance})^2$ so that sources at 0.1 pc would experience $G_0 = 430$. Since the O stars represent the dominant source of FUV radiation, the G_0 values given take into account just the central source and ignore contributions from nearby less massive sources. However, if we were to take into account the 31 candidate OB stars identified in Wolk et al. (2006), the average FUV radiation experienced by a given star would be greater. Higher G_0 values represent a faster photoevaporating effect and most easily affect lower mass stars whose disks are less tightly bound.

If we assume large planet formation occurs in the region of 5-30 AU, for $M_\star = 0.5M_\odot$ or less it would be inhibited over a 2 Myr period in a region where $G_0 = 3000$, though this would only impact the stars minimally if the cluster is < 2 Myr. As an example from Adams et al. (2004), disks around $0.25 M_\odot$ stars would be photoevaporated down to around 14 AU, reducing the reservoir of material for planet formation around the star by half and likely preventing the formation of outer planets. Without velocity dispersion data for the cluster, however, it is difficult to know what kind of orbits the cluster members follow around IRS2 and how much time they actually spend close to this central source. However, if we assume circular orbits for cluster members so that they spend 100% of their time at their projected radial distance, there are 18 JHK_s sources that experience $G_0 \geq 3000$. Of these, 5 sources have detected infrared excess, giving a disk fraction of 27%. However, random sampling of the sources using the disk fraction calculated previously gives a 28% chance of choosing 5 or less excess sources, so that this slightly lower disk fraction is not statistically significant. This result is to be expected since K_s -band excess detects the inner wall of disks which can be found at distances less than 1 AU from the central source so that even if a star’s disk was significantly reduced in size, this lack of disk material would not be noticeable. As an example, Eisner et al. (2008) measured the mass of disks in the ONC versus Taurus and found that the ONC disks are much less massive, indicating that photoevaporation effects from the OB stars in the field, have played a key role in evaporating the outer disks in the ONC.

5.2. Cluster Structure

5.2.1. Azimuthally Averaged Surface Density Profile

The azimuthally averaged surface density profile, or radial profile, of a cluster is a common tool used to probe the decrease in surface density as a function of radius from the central peak (Carpenter et al. 1997; Hillenbrand & Hartmann 1998). King (1962) surveyed 15 globular clusters in order to examine their radial profiles and found a relationship that could be expressed with only the tidal radius and the core radius of a cluster. Hillenbrand & Hartmann (1998) fitted their radial profile for the ONC using such a King profile. Neither the ONC or RCW 38 is a globular cluster in equilibrium which makes the King model less physically significant for this application; however, as RCW 38 shares many similarities with the ONC, it seemed reasonable to determine the King profile parameters for RCW 38 for comparison to the Hillenbrand & Hartmann values.

The radial profile of RCW 38 was made using only the sources detected at K_s with magnitude < 17 and uncertainties < 0.2 . As shown in Figure 14 it is relatively flat inside

the core of the cluster at radial distances less than 0.1 pc and then begins to fall off at further distances. The radial profile can only be examined up to a distance of 0.25 pc from the center of the cluster in order to limit edge effects caused by sampling distances outside the FOV in certain radial directions. This radial profile represents only the sources resolved in this sample, whereas it is possible that there are deeply embedded and extinguished sources that are cluster members but not taken into account in this radial profile. Figure 15 shows a contour map of K_s stellar surface density that illustrates the fairly uniform distribution with only a few small areas of possible subclustering.

The shape of the radial profile in Figure 14 motivates the choice of a flat-topped profile with a power-law drop off to fit the radial profile of the data such as the King model. For regions where the tidal radius is much larger than the core radius (as is generally assumed), the King model can be expressed as:

$$\sigma(r) = \sigma_0 \left[1 + \left(\frac{r}{r_0} \right)^2 \right]^{-1} \quad (3)$$

where r_0 is the core radius of the cluster, and σ_0 is the initial stellar surface density. With $r_c = 0.1$ pc and $\sigma_0 = 5700$ pc⁻², the model provides a reasonable fit to the radial profile of RCW 38 (Fig. 14). Hillenbrand & Hartmann (1998) give best-fit King model parameters of $r_o = 0.164$ pc and $\sigma_o = 5600$ pc⁻² for the ONC. This central density is very close to that of RCW 38 while the scale radius is larger, suggesting that RCW 38 is more centrally concentrated than the ONC.

Because the King model is applicable for globular clusters, observations show that it is not a good fit to the extended outer envelopes of young star clusters in our Galaxy and the LMC and SMC. In this case a modified King model (Elson, Fall, & Freeman 1987; EFF) is a better description:

$$\sigma(r) = \sigma_o \left[1 + \left(\frac{r}{r_o} \right)^2 \right]^{\frac{-\gamma}{2}} \quad (4)$$

where the introduction of the exponent γ allows the more extended nature of Galactic clusters to be fitted. This model differs from the King model in that there is no truncation radius included. For RCW 38 we obtain a best fit with $r_o = 0.1$ pc, $\sigma_o = 5200$ pc⁻² and $\gamma = 1.7$. As in the case of the King model, the EFF model provides a reasonable fit to the data in the flat and power-law fall-off regions.

5.2.2. Nearest Neighbor Distance Analysis

We use a nearest neighbor distance analysis to look for subclustering among close pairs. Our King model (eqn. 3; dashed line in Figure 14) was used to generate a group of 1000 random clusters with the same radial distribution and number of sources as RCW 38. If the RCW 38 distribution of close pairs was significantly different from the Poisson noise models, then we would expect subclustering among close pairs. A nearest neighbor distance histogram of the NACO data with a bin size of 800 AU is compared with the averaged histogram values for these model clusters in Figure 16. The model fits with the data quite well, with almost every bin matching when taking into account the error bars. This shows that there is a fairly low degree of subclustering on a smaller scale, a fact that should be expected given the fairly flat radial profile.

5.2.3. Q Parameter Analysis

Cartwright & Whitworth (2004) use a Q parameter in order to classify star clusters based on the degree a cluster is dominated by either fractal subclustering or a monolithic radial density gradient. They show that a uniform 2D (or unconstrained 3D projected into 2D) distribution gives $Q \sim 0.72$ while a uniform 3D distribution constrained to a spherical volume and projected into 2D gives $Q \sim 0.79$. Thus, spherical clusters with some degree of subclustering are expected to have $Q < 0.79$ while clusters with a smooth radial gradient are expected to have $Q > 0.79$.

The parameter Q is defined as $Q = \frac{m}{s}$ where m is the mean distance from a minimum spanning tree scaled by a factor of $\frac{N-1}{\sqrt{NA}}$ (with N being the number of stars and A being the 2D cluster area) and s is the mean of the two point correlation function measured for all of the stars in the cluster divided by the cluster radius. Using this procedure in order to further characterize the structure of RCW 38, a value of $Q = 0.84$ is found, which places it on the border between clusters that are characterized by a relatively uniform distribution (smooth with a large scale radial gradient) and clusters that show some degree of subclustering. Together with the analysis in the previous section, this result suggests that RCW 38 is quite uniform and does not show strong subclustering.

5.2.4. Larson Analysis

Figure 17 recreates the surface density vs. angular separation plot from Larson (1995). The power law for RCW 38 differs fairly significantly from the original Larson plot and does

not contain the same elbow evident in the Larson plot that is identified as the transition from the clustering to the binary regime. The absence of the elbow is easily explained by the fact that it occurs at an angular separation of 8663 AU, which is at the very high end of the nearest-neighbor histogram in Figure 16 and thus not easily measurable by this smaller field of view. Bate et al. (1998) also explains that we should expect the elbow in the Larson plot to be washed out in a large 3D cluster where the angular separation of many sources can be attributed to projection effects. In addition, from Figure 17 it is clear that RCW 38 is much denser than the Taurus cluster and thus it is possible that different physical processes govern star formation in these regions.

Nakajima et al. (1998) uses a similar Larson analysis on five young star forming regions observed at visible wavelengths, fitting broken power laws to their sample. As a similar break in the Larson plot is not observed in our RCW 38 data, due to the high density, we can only compare the slope found at larger angular separations. Table 4 shows the slopes from Nakajima et al. (1998), where γ_S gives the power-law index at small angular separations while γ_L gives the power-law index at large angular separations, alongside the Larson result for Taurus and the value for RCW 38. The RCW 38 result is intermediate between the values of γ_S and γ_L listed for other regions.

It is difficult to compare the deep near-infrared data from RCW 38 to the V and R band data presented by Nakajima et al. because in those bands there is poor completeness due to the high levels of extinction in the visible band ($A_V \sim 10-30$). Because of the variability in extinction and distance among the clusters surveyed, the mass sensitivities in each region are likely to differ significantly. Allen et al. (2002) show that these factors can affect the Larson plot results significantly in their HST/NICMOS survey of the Ophiuchus cluster.

6. Summary

We have presented high resolution adaptive optics near-infrared imaging (broadband J , H , K_s ; narrowband $1.28 \mu\text{m}$, $2.12 \mu\text{m}$, and $2.17 \mu\text{m}$) of the deeply embedded massive cluster RCW 38, over a field-of-view of ~ 0.5 pc, centered on the O5.5 star IRS2. Our main results are:

1. A total of 360 sources are detected in all three broadbands. Of these, 344 have uncertainties in all bands of < 0.2 mag, and the remainder are removed from the sample. A further seven sources were removed due to contamination from other brighter nearby stars or due to image artifacts, leaving 337 reliable sources. Of these 337, five have $H - K_s$ colors in excess of that expected for T Tauri stars, and are considered to be

protostellar candidates. A comparison to a nearby control field suggests that 15-25 sources are unassociated with the cluster. There are 53 K_s only detected sources, that are most likely to be cluster members due to the small amount of background contamination. These sources could either be highly extinguished T-Tauri stars or protostellar candidates.

2. A $J - H$ vs. $H - K_s$ color-color diagram is used to identify stars with an infrared excess indicative of inner disk emission. In this manner the disk fraction is found to be $29 \pm 3\%$. For comparison to similar data from the ONC, a $0.3 M_\odot$ mass cut and a $(J - H) < 2$ extinction cut was applied to both regions over the same linear area, resulting in disk fractions of $25 \pm 5\%$ for RCW 38 and $42 \pm 8\%$ for the ONC.
3. The central star IRS2 is found to be an equal mass binary of spectral type $\sim O5$ and projected separation 459 AU.
4. Molecular hydrogen line emission, a good tracer of shocked outflow emission, is seen at two locations, from a comparison of the narrowband $2.12 \mu\text{m}$ images with both broadband K_s and narrowband $2.17 \mu\text{m}$ images. At one location this emission has a morphology suggestive of outflow emission, and is associated with a deeply embedded source that is also a hard X-ray source (Wolk et al. 2006).
5. Three candidate photoevaporating disks are identified, with head-tail morphologies, and with stellar-like sources at their heads. Only one lies in close proximity to IRS2 and has a tail pointing directly away from the O star. Although one goal of the study was to identify unresolved proplyds through a careful comparison of narrowband and broadband imaging, this was not possible due to the varying PSF between the bands.
6. The cluster radial density profile is well described by a modified King profile, which is widely used to fit globular clusters. In young star clusters, such a profile breaks down in fitting the extended outer envelopes. This is not a problem for the data presented here, as the FOV is too small to trace the outer envelope region ($\sim 0.25 \text{ pc}$). Nearest neighbor analysis, both directly on the data and on a model density profile that fits the data, show essentially no substructure (sub-clustering). Comparison to other clusters suggests that this is not surprising for our limit FOV. The stellar surface density in the inner region of the clusters is $\sim 5700 \text{ pc}^{-2}$.

There are a number of observational programs on RCW 38 that need to be undertaken in order to improve on this work and that of Wolk et al. (2006). The comparatively low disk fraction of $\sim 29\%$ found using only JHK_s data needs to be confirmed through sensitive

observations in the L -band. The large distance and nebula emission will make these observations difficult. The nature of the protostellar candidates and K_s -band only sources should be further investigated, through sensitive mid-infrared imaging. The OB star candidates identified in Wolk et al. (2006) should be observed with infrared spectroscopy to determine their spectral types. Finally, the age of the cluster needs to be better determined, a difficult task given its extinction and youth.

We thank Joana Ascenso for providing the SOFI data in advance of publication, and for sharing her ISAAC results in advance of publication. We thank the VLT Science Operations team for successfully executing our NACO observations in service mode. Partial support for this work was provided by NASA through contract 1279160 issued by JPL/Caltech, and by NASA contract NAS8-03060. This research has made use of NASA's Astrophysics Data System.

Facilities: VLT:Yepun

REFERENCES

- Adams, F. C., Hollenbach, D., Laughlin, G., & Gorti, U. 2004, *ApJ*, 611, 360
- Adams, F. C., Proszkow, E. M., Fatuzzo, M., & Myers, P. C. 2006, *ApJ*, 641, 504
- Allen, D. A., & Burton, M. G. 1993, *Nature*, 363, 54
- Allen, L., et al. 2007, *Protostars and Planets V*, 361
- Armand, C., Baluteau, J.-P., Joubert, M., Gry, C., & Cox, P. 1996, *A&A*, 306, 593
- Ascenso, J., 2008, Ph.D. Thesis, University of Porto
- Balog, Z., Muzerolle, J., Rieke, G.H., Su, K.Y.L., Young, E.T., & Megeath, S.T. 2007, *ApJ*, 660, 1532
- Baraffe, I., Chabrier, G., Allard, F., & Hauschildt, P. H. 2002, *A&A*, 382, 563
- Bate, R., Clarke, C., & McCaughrean, M. 1998, *MNRAS*, 297, 1163
- Beck, S. C., Fischer, J., & Smith, H. A. 1991, *ApJ*, 383, 336
- Bessell, M. S., & Brett, J. M. 1988, *PASP*, 100, 1134

- Carpenter, J. M., Meyer, M. R., Dougados, C., Strom, S. E., & Hillenbrand, L. A. 1997, *AJ*, 114, 198
- Carpenter, J. M. 2000, *AJ*, 120, 3139
- Cartwright, A., & Whitworth, A. P. 2004, *MNRAS*, 348, 589
- Caswell, J. L., & Haynes, R. F. 1987, *A&A*, 171, 261
- Cheung, L. H., Frogel, J. A., Hauser, M. G., & Gezari, D. Y. 1980, *ApJ*, 240, 74
- Churchwell, E., Wood, D. O. S., Felli, M., & Massi, M. 1987, *ApJ*, 321, 516
- Davis, C. J., et al. 2008, arXiv:0812.3733
- Eisner, J. A., Plambeck, R. L., Carpenter, J. M., Corder, S. A., Qi, C., & Wilner, D. 2008, *ApJ*, 683, 304
- Elson, R. A. W., Fall, S. M., & Freeman, K. C. 1987, *ApJ*, 323, 54
- Feigelson, E., Getman, K., Townsley, L., Garmire, G., Preibisch, T., Grosso, N., Montmerle, T., Muench, A., & McCaughrean, M. 2005, *ApJS*, 160, 379.
- Felli, M., Taylor, G. B., Catarzi, M., Churchwell, E., & Kurtz, S. 1993, *A&AS*, 101, 127
- Frogel, J. A., & Persson, S. E. 1974, *ApJ*, 192, 351
- Gutermuth, R. A., Megeath, S. T., Pipher, J. L., Williams, J. P., Allen, L. E., Myers, P. C., & Raines, S. N. 2005, *ApJ*, 632, 39
- Gutermuth, R. A., Myers, P. C., Megeath, S. T., Allen, L. E., Pipher, J. L., Muzerolle, J., Porras, A., Winston, E., & Fazio, G. 2008, *ApJ*, 674, 336
- Haisch, K. E., Jr., Lada, E. A., & Lada, C. J. 2000, *AJ*, 120, 1396
- Hillenbrand, L. A. 2005, to appear in *A Decade of Discovery: Planets around Other Stars*, ed. M. Livio (Baltimore: STScI), ArXiv Astrophysics e-prints, arXiv:astro-ph/0511083
- Hillenbrand, L. A., & Hartmann, L. W. 1998, *ApJ*, 492, 540
- Hollenbach, D., Johnstone, D., Lizano, S., & Shu, F. 1994, *ApJ*, 428, 654
- King, I. 1962, *AJ*, 67, 471
- Kristensen, L. E., Gustafsson, M., Field, D., Callejo, G., Lemaire, J. L., Vannier, L., & Pineau des Forêts, G. 2003, *A&A*, 412, 727

- Lada, C. J., Muench, A. A., Haisch, K. E., Jr., Lada, E. A., Alves, J. F., Tollestrup, E. V., & Willner, S. P. 2000, *AJ*, 120, 3162
- Lada, C. J., & Lada, E. A. 2003, *ARA&A*, 41, 57
- Lada, C. J., & Adams, F. C. 1992, *ApJ*, 393, 278
- Landsman, W. B. 1993, *Astronomical Data Analysis Software and Systems II*, 52, 246
- Laques, P., & Vidal, J. L. 1979, *A&A*, 73, 97
- Larson, R. B. 1995, *MNRAS*, 272, 213
- Lenzen, R., et al. 2003, *Proc. SPIE*, 4841, 944
- Martins, F., Schaerer, D., Hillier, D. J., Meynadier, F., Heydari-Malayeri, M., & Walborn, N. R. 2005, *A&A*, 441, 735
- McCaughrean, M. J., & Mac Low, M.-M. 1997, *AJ*, 113, 391
- Menten, K.M., Reid, M.J., Forbrich, J., & Brunthaler, A. 2007, *A&A*, 474, 515
- Meyer, M. R., Calvet, N., & Hillenbrand, L. A. 1997, *AJ*, 114, 288
- Meyer, B. S., & Clayton, D. D. 2000, *Space Science Reviews*, 92, 133
- Mokiem, M. R., Martín-Hernández, N. L., Lenorzer, A., de Koter, A., & Tielens, A. G. G. M. 2004, *A&A*, 419, 319
- Muench, A. A., Lada, E. A., Lada, C. J., & Alves, J. 2002, *ApJ*, 573, 366
- Nakajima, Y., Tachihara, K., Hanawa, T., & Nakano, M. 1998, *ApJ*, 497, 721
- Nürnbergger, D. E. A., & Petr-Gotzens, M. G. 2002, *A&A*, 382, 537
- O'dell, C. R., Wen, Z., & Hu, X. 1993, *ApJ*, 410, 696
- O'dell, C. R. 1998, *AJ*, 115, 263
- Panagia, N. 1973, *AJ*, 78, 929
- Porras, A., Christopher, M., Allen, L., Di Francesco, J., Megeath, S. T., & Myers, P. C. 2003, *AJ*, 126, 1916
- Rieke, G. H., & Lebofsky, M. J. 1985, *ApJ*, 288, 618

Rousset, G., et al. 2003, Proc. SPIE, 4839, 140

Smith, C. H., et al. 1999, MNRAS, 303, 367

Vigil, M., 2004, M.Sc. Thesis, Massachusetts Institute of Technology

Wilson, T. L., Mezger, P. G., Gardner, F. F., & Milne, D. K. 1970, A&A, 6, 364

Wolk, S. J., Bourke, T. L., Smith, R. K., Spitzbart, B., & Alves, J. 2002, ApJ, 580, L161

Wolk, S. J., Spitzbart, B. D., Bourke, T. L., & Alves, J. 2006, AJ, 132, 1100

Table 1. DITs (Detector Integration Times) and NDITs for observations in each band.

Band	DIT (s)	NDIT
J	4.0	16
H	0.75	80
K_s	0.50	120
NB_2.12	10.0	14
NB_2.17	10.0	12
NB_1.28	90.0	4

Table 2. Number of detected sources.

Band	Detections with 0.2 magnitude uncertainty cap
J	355
H	420
K_s	465
JHK_s All	344

Table 3. Infrared Photometry of sources detected with magnitude uncertainties < 0.2 .

Source Number	R.A. (J2000)	Dec. (J2000)	J	J_{err}	H	H_{err}	K_s	$(K_s)_{\text{err}}$	Notes
1	8 59 2.49	-47 30 20.7	14.09	0.06	
2	8 59 2.50	-47 30 52.6	15.02	0.09	
3	8 59 2.55	-47 30 39.9	14.41	0.06	
4	8 59 2.56	-47 30 46.2	12.08	0.02	
5	8 59 2.57	-47 30 53.5	13.09	0.03	
6	8 59 2.60	-47 30 31.7	13.35	0.04	
7	8 59 2.62	-47 30 35.2	12.86	0.03	
8	8 59 2.63	-47 30 28.7	15.07	0.08	
9	8 59 2.66	-47 30 42.3	13.52	0.04	
10	8 59 2.67	-47 30 57.4	15.68	0.14	
11	8 59 2.67	-47 30 21.1	14.83	0.08	
12	8 59 2.74	-47 30 43.4	17.72	0.07	15.32	0.09	
13	8 59 2.76	-47 30 53.8	17.28	0.13	14.95	0.07	
14	8 59 2.78	-47 30 46.8	14.97	0.02	13.61	0.02	12.65	0.03	e
15	8 59 2.83	-47 30 34.0	16.49	0.15	
16	8 59 2.89	-47 31 6.5	15.25	0.10	
17	8 59 2.91	-47 30 30.8	16.97	0.05	15.11	0.05	13.83	0.04	e
18	8 59 2.92	-47 31 2.1	15.01	0.02	13.44	0.02	12.36	0.02	e
19	8 59 2.93	-47 30 54.1	12.27	0.01	10.51	0.01	9.81	0.01	
20	8 59 2.93	-47 30 54.1	12.14	0.02	
21	8 59 2.97	-47 30 39.8	15.10	0.02	13.71	0.02	12.85	0.03	e
22	8 59 2.98	-47 30 51.7	17.88	0.10	15.90	0.06	14.12	0.05	p
23	8 59 2.99	-47 31 0.9	16.78	0.10	15.49	0.10	
24	8 59 3.00	-47 30 44.4	16.25	0.03	13.54	0.02	11.00	0.01	p
25	8 59 3.02	-47 30 35.6	14.88	0.02	12.67	0.01	11.47	0.01	

Note. — In the Notes column, ‘e’ refers to those sources with an infrared excess, ‘p’ to protostars, which are sources with an excess greater than of that expected of a reddened T Tauri stars, and ‘x’

to sources that have $J - H < 1$ and whose photometry is incorrect, for reasons described in the text. Units of right ascension are hours, minutes and seconds, and units of declination are degrees, arcminutes, and arcseconds. Units of J , J_{err} , H , H_{err} , K_s , $(K_s)_{\text{err}}$ are magnitudes. Table 3 is published in its entirety in the electronic edition of the *Astronomical Journal*. A portion is shown here for guidance regarding its form and content.

Table 4. Slopes for Larson plots for Taurus (Larson 1995) and the clusters surveyed by Nakajima et al. (1998). γ_S gives the power-law index at shorter angular separations while γ_L gives the power-law index at longer angular separations.

Region	γ_S	γ_L
Orion OB	-1.6 ± 0.4	-0.15 ± 0.02
Orion A	...	-0.23 ± 0.02
Orion B	...	-0.69 ± 0.01
ρ Oph	-2.5 ± 0.3	-0.36 ± 0.06
Cha I	-2.1 ± 0.2	-0.57 ± 0.04
Cha	-2.4 ± 0.5	-0.55 ± 0.03
Vela	...	-0.61 ± 0.02
Lupus	-2.2 ± 0.4	-0.82 ± 0.13
Taurus	-2.15	-0.62
RCW 38	...	-1.32

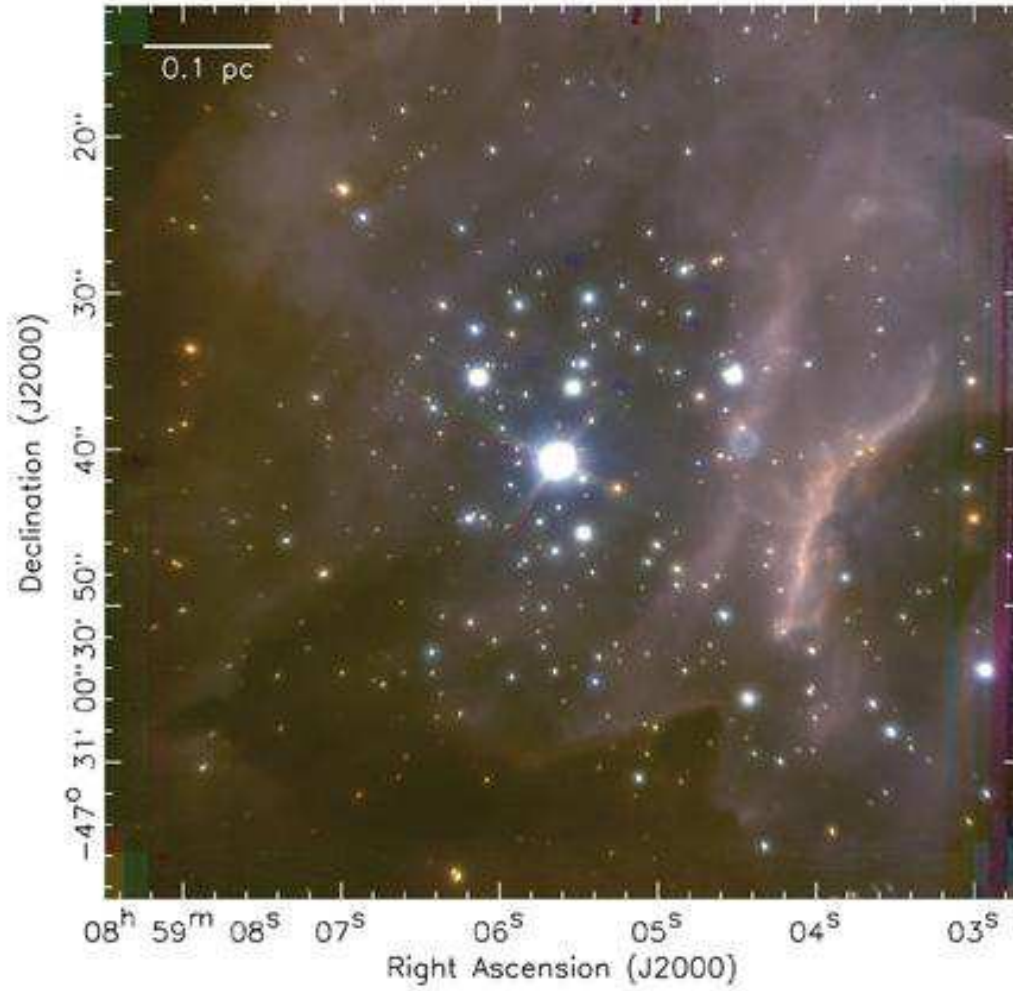


Fig. 1.— Color composite image of RCW 38 through J (blue), H (green), and K_s (red) filters. The bright star in the center is IRS2. The blue sources to the north and south of IRS2 are J-band artifacts, as is the ring-like structure to the west of IRS2 in the nebulous filament (known as IRS1 from mid-infrared wavelengths).

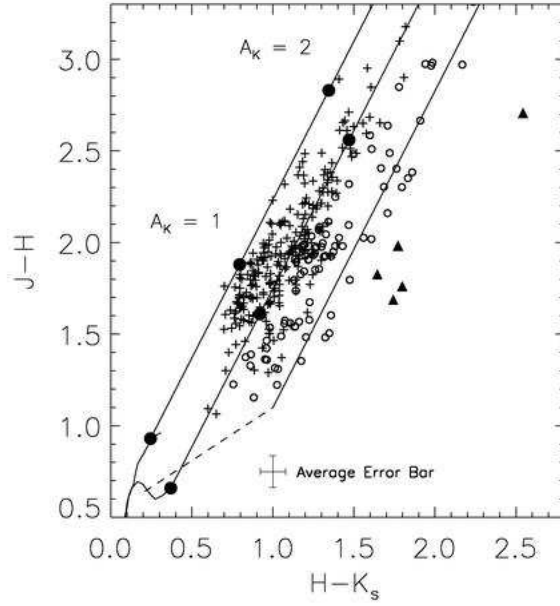


Fig. 2.— Color-Color Diagram for the NACO field. Plotted are the 337 sources detected in JHK_s as discussed in Section 4.1. Reddened sources with $\sigma < 0.2$ are displayed with crosses. Open circles indicate K_s -band excess sources identified by discarding sources within 1σ of the lowest reddening vector in either dimension. Filled triangles represent protostellar candidates (Class I sources) or extreme CTTS's (Lada & Adams 1992 or Carpenter et al. 1997). Upper and lower reddening vectors are from Rieke & Lebofsky (1985) and plotted as solid lines for an M5 giant (Bessell & Brett 1988) and M5 dwarf (B. Patten 2004, private communication) respectively. Reddening of $A_K = 1$ and 2 is indicated by the filled circles. The classical T-Tauri stars (CTTS) locus from Meyer et al. (1997) is plotted as a dotted line. Some of the sources are identified as non-excess sources despite appearing in quite far into the region where they would appear to be excess sources, due to greater than average errors that overlap with the non-excess region to the left of the first reddening vector. These sources are all faint sources, and are evenly distributed at different radii from IRS2.

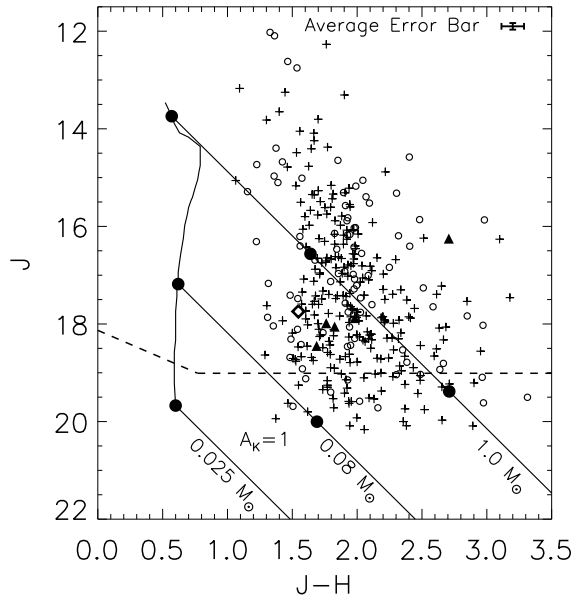


Fig. 3.— Color-Magnitude diagram for NACO field. Symbols as in Figure 2: reddened JHK_s sources are crosses, K_s -band excess sources are circles, and candidate protostars are triangles. The single black diamond indicates the only source detected in J and H that was not detected in K_s (thus our sample is not biased towards detected excess in K_s). Completeness limits for J and H are represented as dashed lines. The curved line at left is the unreddened 1 Myr pre-main-sequence isochrone from Baraffe et al. (2002) with reddening vectors (Rieke & Lebofsky 1985) at $0.025 M_{\odot}$, $0.08 M_{\odot}$, and $1.0 M_{\odot}$ shown as downward sloping lines. From this diagram it is clear that the cluster is reddened by around $A_K = 1$. Despite the surrounding differential reddening that exists due to the nebulosity, the cluster is surrounded by a bubble of nebulosity with the central region evacuated due to the wind from the O stars. This causes the overall reddening to be fairly constant over the sources within the cluster core.

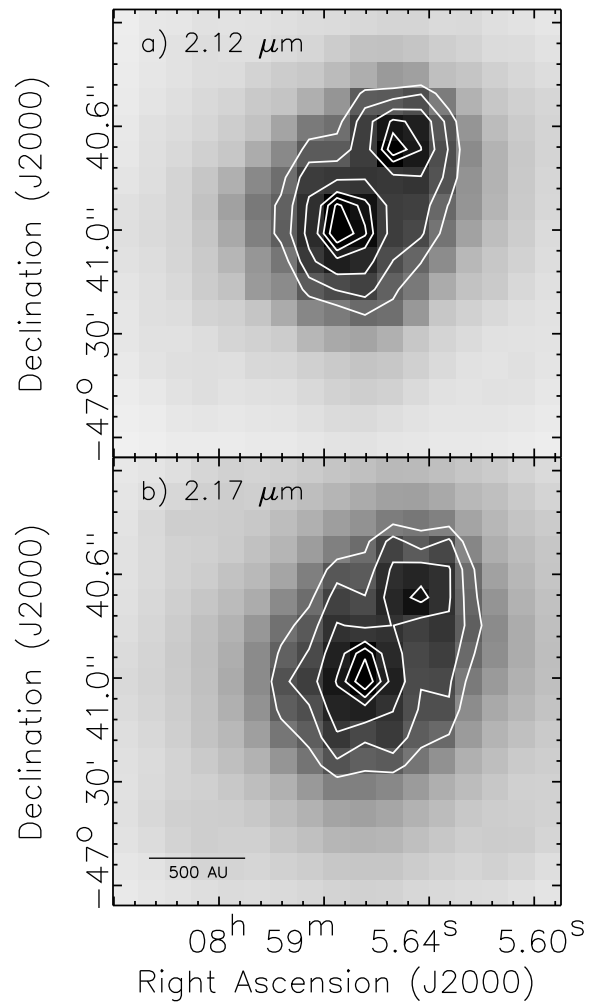


Fig. 4.— a) Magnified image of IRS2 from the narrowband 2.12 μm image. Contours are plotted at 60, 70, 80, 90, 95 and 100% of the peak flux in arbitrary units. b) Magnified image of IRS2 from the narrowband 2.17 μm image. Contour levels are the same as in a).

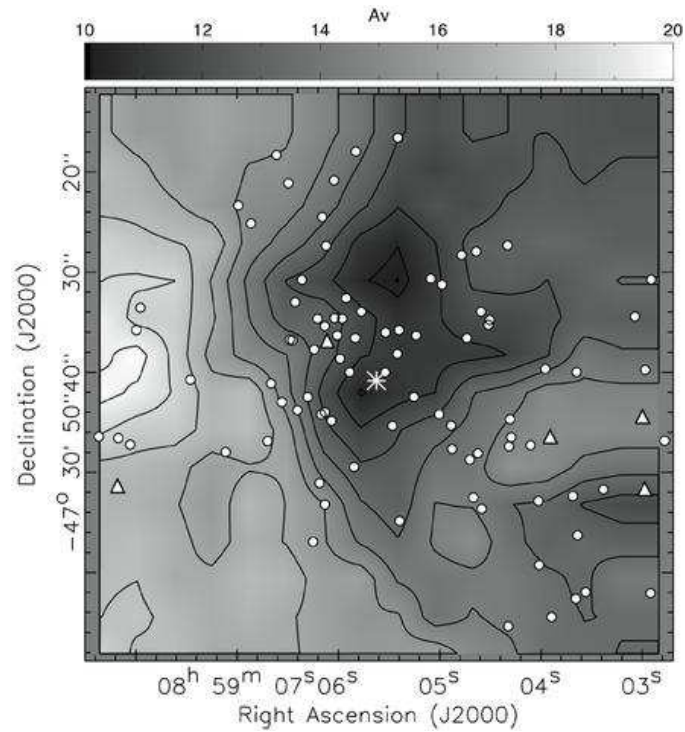


Fig. 5.— Shaded extinction contour map for the NACO FOV. White areas indicate areas of higher extinction, expressed in a linear scaling where black represents $A_V = 10$ and white represents $A_V = 20$. Contours are given for $\Delta A_V = 1$, starting at $A_V = 10$. K_s -band excess sources and potential protostellar candidates as identified in Figure 2 are overplotted using the same symbols as that figure (white circles and white triangles respectively). The bright central source IRS2 is overplotted as a white star.

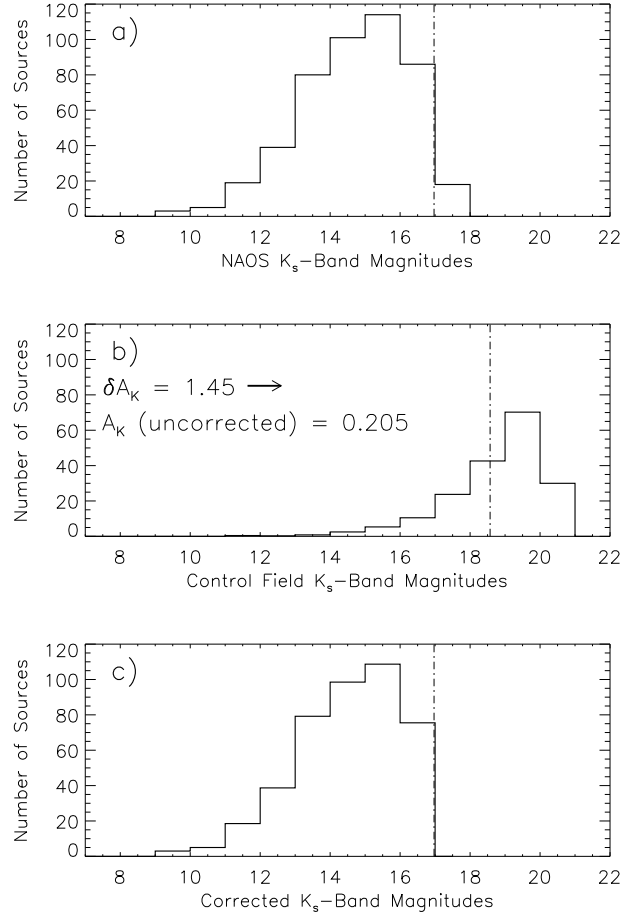


Fig. 6.— a) Histogram of NACO K_s -band magnitudes divided into bins of 1 magnitude. All sources detected at K_s , regardless of detectability at J or H , are included. The dotted line represents the 90% completeness limit. b) Histogram of SOFI control field K_s -band magnitudes divided in bins of 1 magnitude and normalized by the ratio between the NACO FOV and the SOFI FOV. The dotted line represents the 90% completeness limit. The histogram has been shifted to the right by the amount δA_K as described in the text. c) NACO histogram corrected by subtracting the SOFI control field histogram. Only bins within the 90% differential completeness limit for the NACO measurements are included.

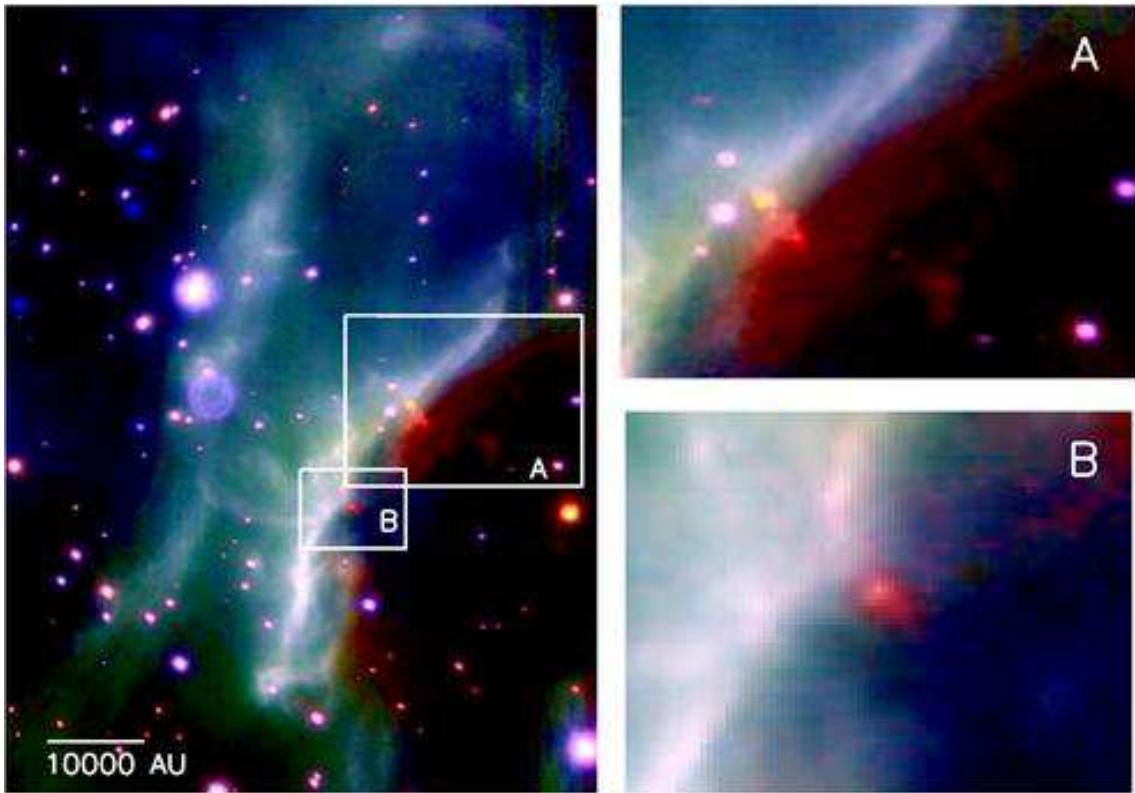


Fig. 7.— Molecular hydrogen emission in the 1-0 S(1) line is revealed in these images, which combine narrow-band images at $2.12 \mu\text{m}$ (red), $2.17 \mu\text{m}$ (green), and $1.28 \mu\text{m}$ (blue). In the left panel is shown the IRS 1 ridge region, and on the right are shown zoomed in regions A and B. The H_2 emission is shown in red.

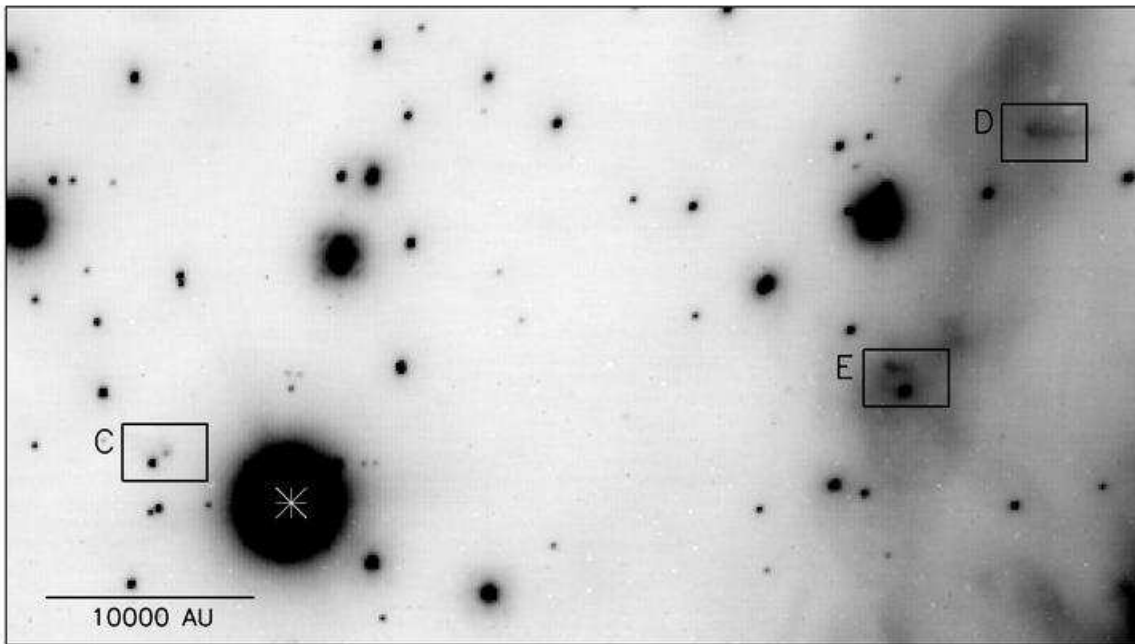


Fig. 8.— Finding chart for proplyd-like objects. The image is the narrowband $2.17 \mu\text{m}$ image, and the three proplyd-like objects shown in more detail in Figs. 9-11 are indicated by the boxes marked C, D and E. IRS2 is indicated with an asterix.

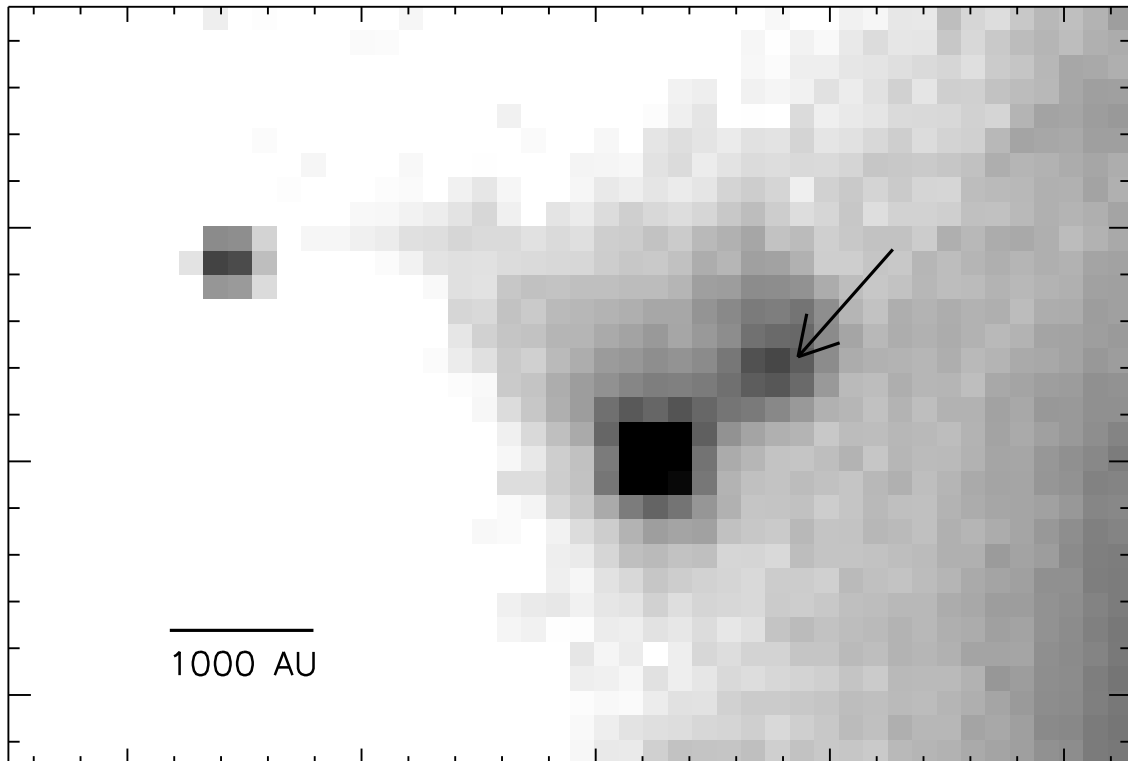


Fig. 9.— Image at $2.12 \mu\text{m}$ showing a candidate proplyd with a tail near IRS2. Identified as Region C in Figure 8. The arrow points to the head of this globule, with the tail stretching leftwards and slight upwards, away from the location of IRS2.

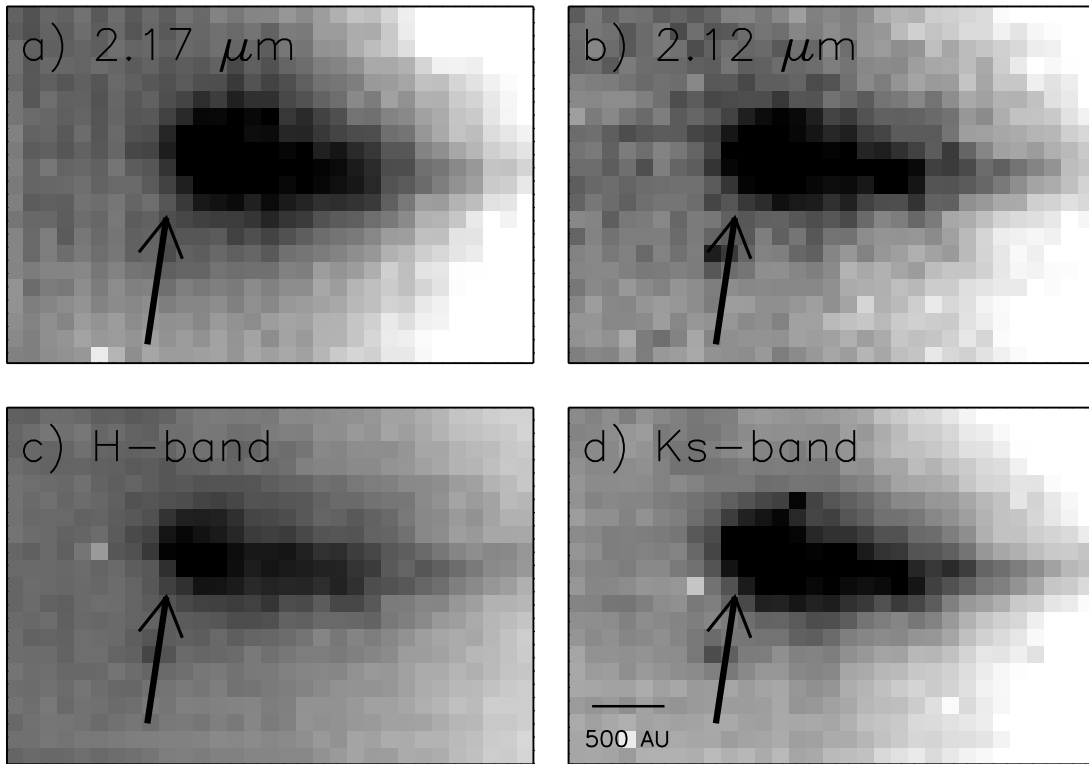


Fig. 10.— Images in four bands (as noted) of a proplyd candidate with tail. Identified as Region D in Figure 8.

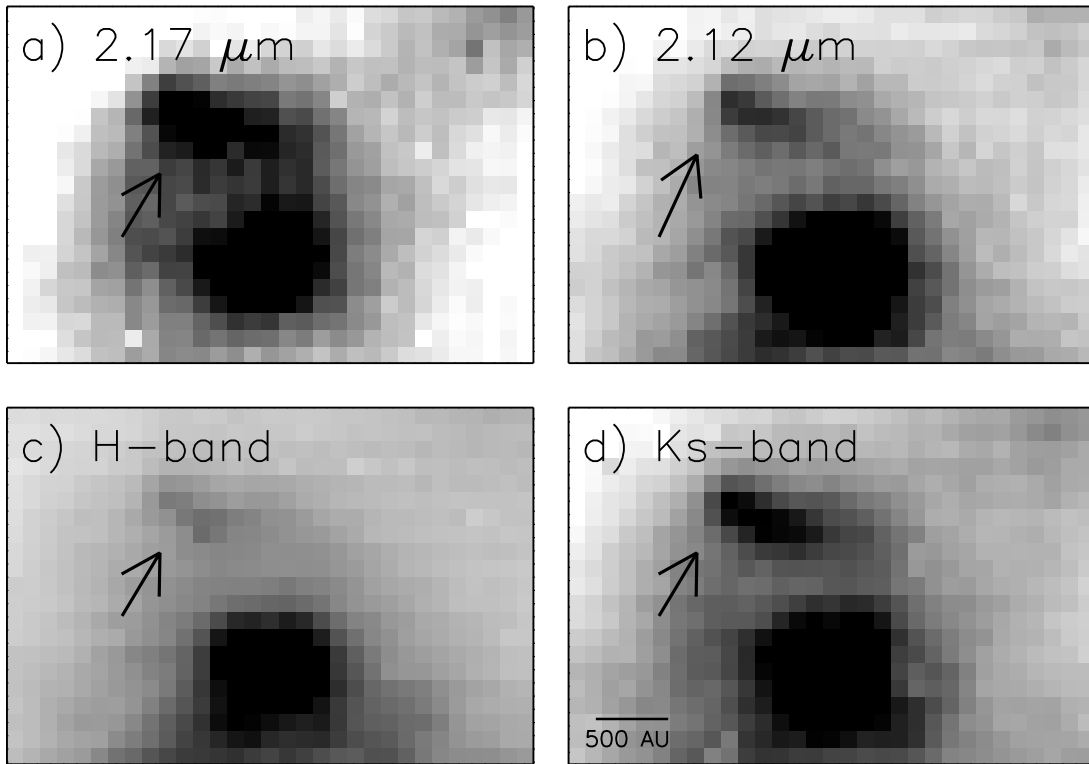


Fig. 11.— Images in four bands (as noted) of a protoplanetary candidate with tail. Identified as Region E in Figure 8. The arrows point to the head of the globule.

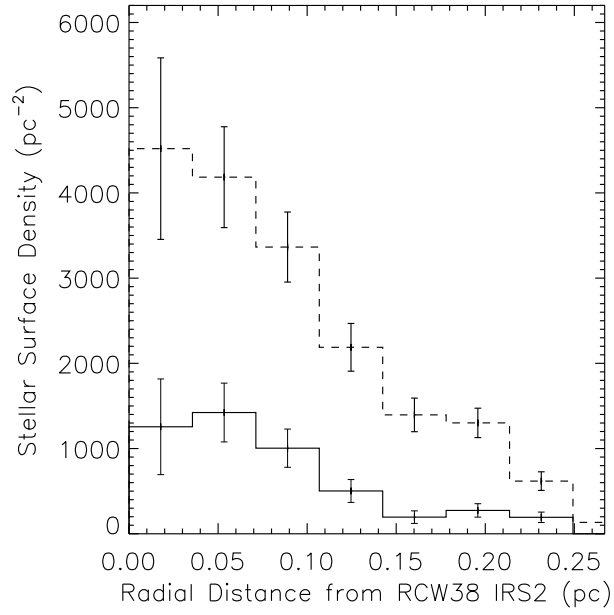


Fig. 12.— Radial surface density plot IRS2. Bin size is $4''$. The dashed line indicates all JHK_s sources and the solid line is K_s -band excess sources from Figure 2.

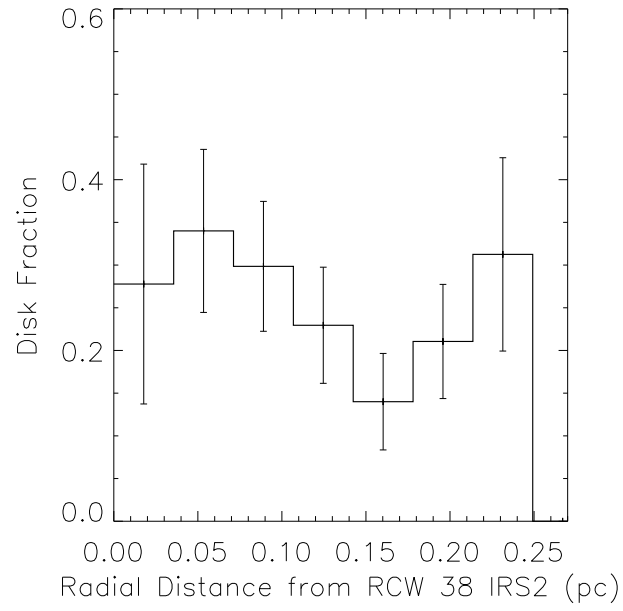


Fig. 13.— Disk fraction vs. radial distance from IRS2. Bin size is about $4''$.

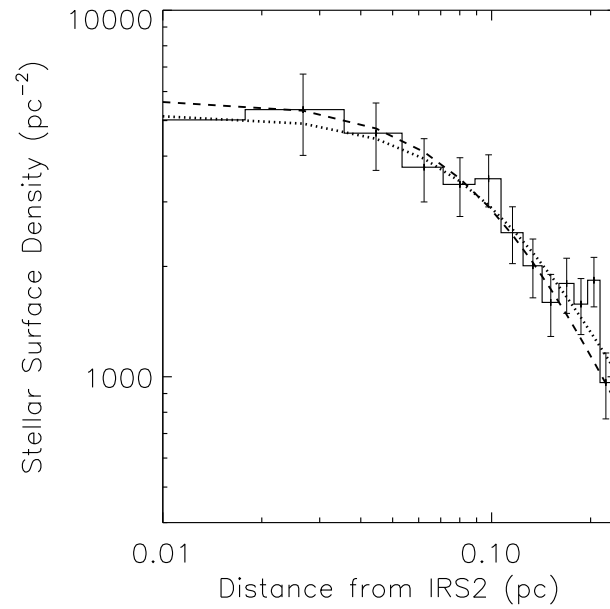


Fig. 14.— Radial stellar surface density plot for RCW 38 centered on IRS2 using NACO data. Bin size is about 0.02 pc ($2''.5$). The stellar surface density is computed for all sources detected with $K < 17$ with $\sigma < 0.2$. The dashed line represents the fitted King model (eqn. 3) while the dotted line represents the fitted Elson et al. (1987; EFF) model (eqn. 4).

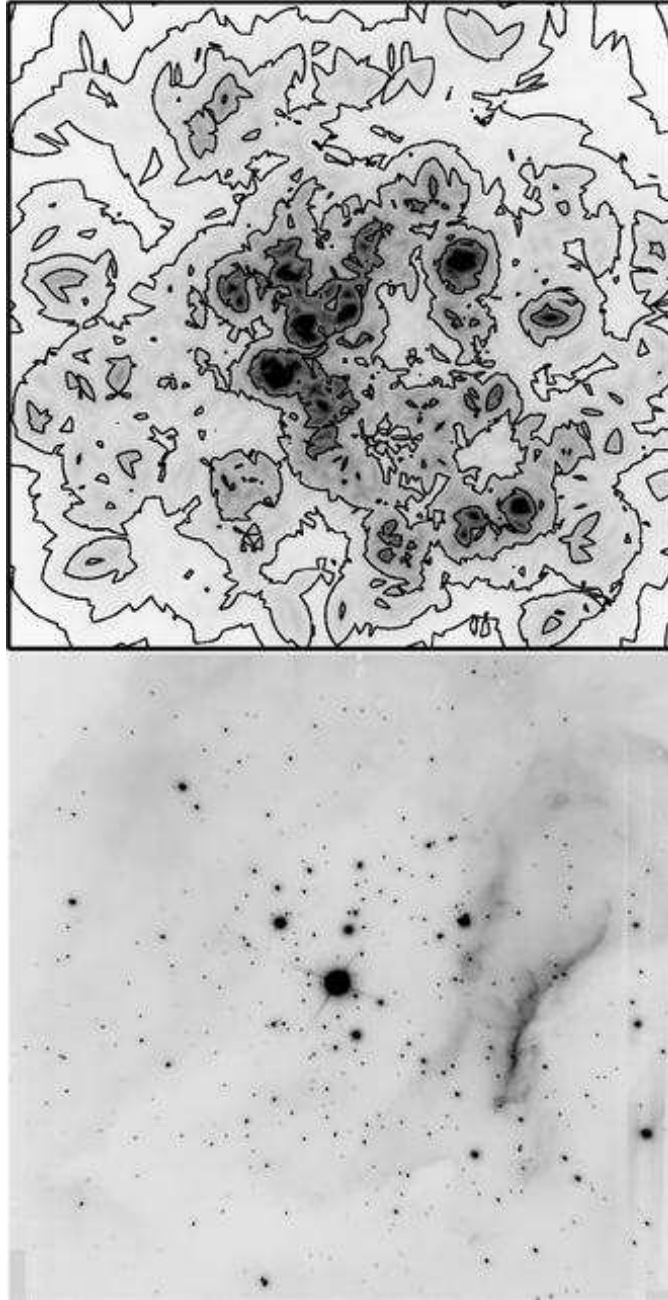


Fig. 15.— Stellar surface density plot. The contours of K_s stellar surface densities for sources with $K < 17$ and $\sigma < 0.2$ are shown in the upper image. The contours represent stellar surface densities of 30, 100, 500, 1000, 2500, 5000, 10000, 20000, and 25000 stars pc^{-2} . Densities are computed using 5 nearest neighbors. For reference, in the lower panel is shown the same FOV using the K_s band image.

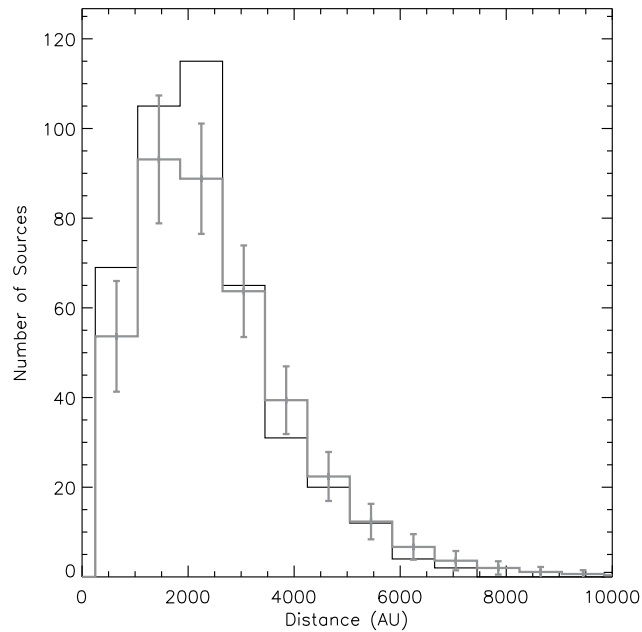


Fig. 16.— Nearest neighbor histogram. Black represents NACO data (using sources with $K < 17$ and $\sigma < 0.2$) and grey is the average of 1000 randomly generated clusters with the same radial profile as shown in Figure 14. Error bars represent the standard deviation of the random averaged clusters in each bin. Bin size is 800 AU. As a note, the two-point correlation function (TPCF) of this same data set yields nearly identical results, so it is not included here. Since the data does not deviate significantly from the model (where sources are randomly distributed for the given radial profile), it is consistent with the model that no major substructuring exists in this FOV. This is as expected because the radial density plot in Figure 14 is essentially flat over most of the region.

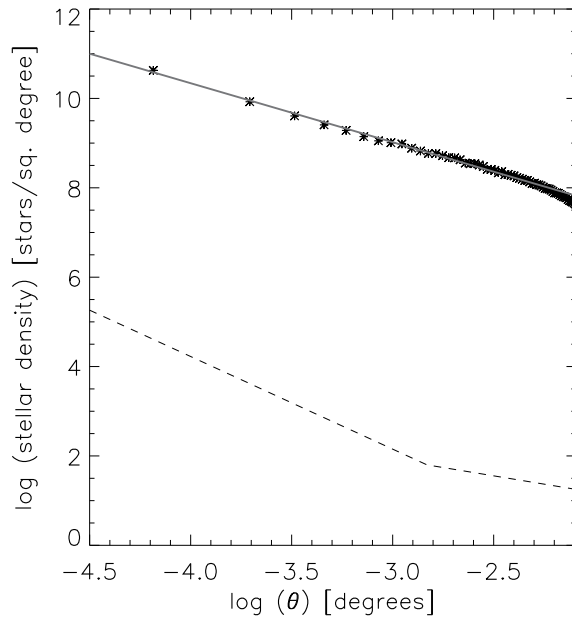


Fig. 17.— Surface density of companions as a function of angular separation (after Larson 1995). The Larson result, scaled to the same distance, is shown as a dashed line (the original Larson result shows an elbow at around $\log \theta = -1.75$ which translates to $\log \theta = -2.83$, for the distance to RCW 38 of 1.7 kpc, cf. 140 pc for Taurus). The grey line shows a power law of -1.32 which is significantly different from the -2.15 power law for the binary regime and -0.62 power law for the clustering regime measured in Larson (1995).